

1 Molecular dynamics study of interfacial stress transfer  
2 in graphene-oxide cementitious composites

Ding Fan<sup>a</sup>, Leo Lue<sup>b</sup>, Shangtong Yang<sup>a,\*</sup>

<sup>a</sup> *Department of Civil and Environmental Engineering, University of Strathclyde, James Weir Building, 75 Montrose Street, Glasgow G1 1XJ, United Kingdom.*

<sup>b</sup> *Department of Chemical and Process Engineering, University of Strathclyde, James Weir Building, 75 Montrose Street, Glasgow G1 1XJ, United Kingdom.*

---

**Abstract**

Graphene oxide has been recently used to create cementitious nanocomposites with enhanced mechanical properties and durability. To examine the improvement on the mechanical properties of cement by adding graphene oxide, the understanding of the interfacial stress transfer is a key. In this work, pull-out tests were carried out using molecular dynamics simulations, incorporating cement and graphene oxide, to determine the shearing mechanism at the interface. For the first time, the shear stress-displacement curve, which represents the bond-slip relation has been calculated for a graphene oxide / cement nanocomposite at the molecular scale. This relation is significant and essential in multi-scale numerical modeling as it defines the mechanical properties for the interface elements. A yielding-like phase is found prior to the shear strength and a roughly bilinear softening phase (i.e. fracture/damage). Furthermore, the shear strength has been found in the range of  $647.58 \pm 91.18$  MPa, based on different repeated simulations, which indicates strong

---

\*Corresponding author.

*Email address:* shangtong.yang@strath.ac.uk (Shangtong Yang)

interfacial bonding strength in graphene oxide cement.

*Keywords:* graphene oxide, cementitious materials, interfacial stress transfer, molecular dynamics.

---

## 3 1. Introduction

4 Cementitious material, which is composed of mainly cement and possibly  
5 a mixture of fly ash, slag, limestone fines, silica fume, etc., is the most used  
6 construction material in the world. Since the invention of modern cement,  
7 there has been considerable research to improve its characteristics in terms of  
8 toughness [1], strength [2, 3], and durability [4, 5]. Other than the direct im-  
9 provement of cement itself, a variety of fibers have been added to cement to  
10 enhance the properties of the cementitious materials. More recently, thanks  
11 to the rapid development of nanotechnology, a new dimension of research  
12 has been initiated in cementitious nanocomposites, investigating the prop-  
13 erties of cement containing nanomaterials such as nanoparticles composed  
14 of metal oxide or silica [6], nanofibers [7], and nanotubes [8]. It has been  
15 shown that these nano-inclusions can significantly improve the compressive  
16 strength, flexural strength, Youngs modulus and other material properties of  
17 cement. Since the first successful isolation of the individual graphene sheet  
18 [9], graphene has been considered as an ideal nano-inclusion in numerous ma-  
19 terials including cement [10]; however, the direct application of graphene in  
20 forming cementitious nanocomposites is currently limited due to dispersion  
21 issues.

22 Graphene oxide (GO), the oxidized form of graphene, has started to be-  
23 come accepted as a suitable inclusion in cement for its combined advan-

24 tages of enhancement in mechanical properties, durability, and dispersibility  
 25 [11, 12, 13]. For example, GO cement at 28 days with 0.06 wt% of GO  
 26 content can increase compressive strength by 72.7%, and 0.04 wt% of GO  
 27 content can increase the flexural strength by 67.1% [12]. As a 2-D structure,  
 28 GO has a large aspect ratio, which could lead to reduced permeability and  
 29 chloride ingress for optimal durability of the composite cementitious materi-  
 30 als [13]. This shows that GO has significant potential in enhancing a variety  
 31 of properties of cement. Scanning electron microscopy (SEM), x-ray diffrac-  
 32 tion (XRD), atomic force microscopy (AFM) has been used by Alkhateb  
 33 and co-workers [10] to obtain the physical and chemical properties and res-  
 34 onant ultrasound spectroscopy (RUS) for certain mechanical properties of  
 35 GO cement. Lv and co-workers [14] examined the effects of graphene oxide  
 36 on the cement hydration process in terms of the crystals shapes and their  
 37 formation with different dosages of GO inclusions. They found that cement  
 38 formed flower-like structures on the surface when the dosages of GO ranged  
 39 from 0.01% to 0.04%; however, it formed polyhedral structures from rod-like  
 40 crystals on the surface when the dosages of GO exceeded 0.05%. Moreover,  
 41 XRD tests showed [14] the GO sheets generate more crystalline phases such  
 42 as calcium hydroxide, ettringite, and monosulfoaluminate in cement.

43 Despite the promising future of incorporating GO in forming cementitious  
 44 nanocomposites for optimal engineering properties, the current research of  
 45 GO cement is still at a very early stage. To investigate the massive increase  
 46 in the mechanical properties of GO cement, it is necessary to study the inter-  
 47 facial stress transferring mechanisms between the cement and the GO. The  
 48 stress transferring mechanisms and effectiveness at the interfaces controls the

49 global mechanical performance of the GO cement. Molecular dynamics (MD)  
50 provides unique insight into the mechanical performance of cementitious ma-  
51 terials and nanocomposites at the nanoscale. MD can be used to calculate the  
52 deformation, the stress, and various molecular properties of cement systems  
53 [15, 16, 17]. A molecular approach to determining the mechanical properties  
54 of cementitious materials is extremely helpful when physical nanoscale exper-  
55 iments are not widely available. In GO cement, the GO is mixed and reacted  
56 with the main binding phase of cement — a calcium-silicate-hydrate (C-S-H)  
57 gel. Alkhateb et al. [10] has investigated the interfacial stress transfer for GO  
58 cement. In their study, a cell containing C-S-H with a layer of GO in the mid-  
59 dle was constructed, and the COMPASS force field was applied. A pull-out  
60 test was conducted, and the interfacial strengths were calculated. However,  
61 the structure of C-S-H was not clear, and the full stress-strain curve, which  
62 represents the complete stress transferring behavior, was not shown. Li and  
63 co-workers [18] simulated the pull-out test of carbon nanotube polymer with  
64 MD and produced the full shear stress and displacement relation at the in-  
65 terface between the carbon nanotube and the polymer. Ding et al. [19]  
66 investigated the effects of GO sheets in poly(vinyl alcohol)/GO composites  
67 by using MD and found that the degree of oxidation of the GO sheet in-  
68 fluenced the strength of interfacial binding characteristics between GO and  
69 the polymer. Liu et al. [20] examined the interfacial mechanical properties  
70 of wrinkled GO/polyethylene and GO/PMMA composites by pull-out tests  
71 with MD; it has been found that the pull-out velocity of the wrinkled GO  
72 sheet has a great impact on the interfacial stress transfer capacity for both  
73 types of composites and the wrinkled shape of GO can also enhance the inter-

74 facial mechanical properties. To the best knowledge of the authors, however,  
75 there is very little research in modelling the interfacial mechanical properties  
76 of GO/cement composite and none in deriving the complete interfacial shear  
77 stress/displacement relation with MD.

78 This paper attempts to model the interfacial stress transferring mecha-  
79 nism in GO reinforced cement using MD and derive the full shearing stress  
80 displacement curve by the pull-out test. The C-S-H structure used is based  
81 on 11 Å tobermorite, and the Lerf-Klinowski model for the GO structure  
82 is employed with random distribution of the functional groups. ReaxFF is  
83 used to represent the interatomic interactions in the MD simulation. The  
84 GO sheet is pulled out of the C-S-H and the full stress displacement curve  
85 is obtained based on which the complete stress transferring mechanism is  
86 discussed. The sensitivity of the pulling rate on the results is investigated  
87 and for each pulling rate, three tests/simulations are carried out to ensure  
88 repeatability and reliability. The interfacial shear stress is then calculated as  
89 a function of pull-out displacement. A yielding-like stage, between the linear  
90 stress increase and the stress softening, is identified. The elastic-plastic-  
91 fracture phenomenon has been first observed at nanoscale for GO cement  
92 composite and will have significant impact on engineering mechanical prop-  
93 erties. The energies of the interface between GO and C-S-H, and the carbon  
94 atoms from the GO sheet are also calculated and discussed. The results from  
95 this model are highly complementary to finite element multi-scale modelling  
96 on GO cement composites. In order to accurately simulate the mechanical  
97 behavior of the GO cement, especially at the meso- and micro-scale, the in-  
98 terfacial properties between GO and cement are necessary. However, such

99 properties are extremely difficult to determine from experimental tests. This  
100 has motivated the work in this paper.

101 The remainder of this paper is structured as follows. In Section 2, we  
102 present the formulation of the model which covers the molecular structure  
103 of the composite, the interatomic force field, and the loading protocol for  
104 determining the interfacial mechanical properties. In Section 3, we present  
105 results of the load-displacement relationship for different loading rates, as well  
106 as the energies for both the interface and the carbon atoms. We then analyze  
107 the interfacial mechanism and calculate the shear stress development over the  
108 pull-out displacement. Finally, the conclusions of this work are summarized  
109 in Section 4.

## 110 2. Model Construction

111 The structure of C-S-H analyzed in this paper is constructed based on the  
112 11 Å tobermorite structure reported in [21]. The structure of C-S-H is consid-  
113 ered very similar to that of 11 Å tobermorite [22] with two main differences:  
114 the calcium/silicon ratio and the silicate chain length. Researchers have  
115 been trying to determine the molecular structure for C-S-H materials based  
116 on 11 Å or 14 Å Tobermorite, but there are still few widely acknowledged  
117 models. Pellenq et al. [23] have derived perhaps the first realistic molecular  
118 model for C-S-H with MD, which represented the first-step forward towards  
119 modelling the mechanical properties of C-S-H. However, the several short-  
120 comings of the model have been pointed out, such as a few aspects of the  
121 structure do not match with the general observations on crystalline calcium  
122 silicate hydrates, (e.g., the coordination of Ca-O) [24]. In this paper, the

123 well-understood 11 Å tobermorite structure is used as the structure of C-S-  
 124 H, which is believed reasonable, since the interface between the C-S-H and  
 125 GO is the focus of the research.

126 The GO structure in this paper is based on the Lerf-Klinowski GO model  
 127 [25] with the distortions neglected and the carbon plane structurally unaf-  
 128 fected, as shown in Figure 1. In this model, the functional groups, includ-  
 129 ing epoxy and hydroxyl, are distributed randomly [26] to avoid the energy  
 130 reduction of GO sheet due to the gathering of the functional groups [27].  
 131 Generally, the range of oxidation varies from a C/O ratio of 4:1 to 2:1 [28].  
 132 In this model, the ratio of C/O is set to 3.2:1. The distribution of oxygen  
 133 atoms is derived by Dyer, Thamwattana and Jalili [29], which was based on  
 134 the density functional theory (DFT) analysis performed by Yan and Chou  
 135 [27]. An epoxy functional group is a single oxygen atom bonded with two  
 136 neighboring carbon atoms in the carbon plane. The C-O bond length at  
 137 relaxation is found 1.44 Å. The C-C bond is stretched to 1.51 Å and the two  
 138 carbon atoms move out of the plane by 0.34 Å. Therefore, the oxygen atom  
 139 in an epoxy group is deduced at a perpendicular distance of from the car-  
 140 bon basal plane. The hydroxyl functional group is constructed as the OH  
 141 group bonds to certain carbon atoms. The O-H bond length is found to be  
 142 0.98 Å, and the angle of C-O-H bond is 107.9°. The attached carbon atom  
 143 is distorted out of the plane by 0.37 Å. The hydrogen and oxygen atoms  
 144 are placed at the same plane perpendicular to the basal plane for simplicity.  
 145 Therefore, the oxygen atoms in hydroxyl groups stay at perpendicular dis-  
 146 tance of  $1.44 \sin 107.9^\circ + 0.37 = 1.74$  Å from the basal plane. The average  
 147 of the distance between the carbon sheet and oxygen atoms can be simply

148 calculated as  $(1.57 + 1.74)/2 \text{ \AA}$ .

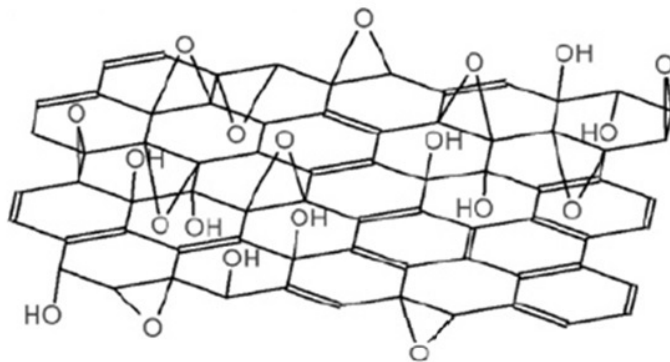


Figure 1: The Lerf-Klinowski model for graphene oxide (reproduced from [30]).

149 The interface between the GO sheet and the C-S-H matrix is difficult  
 150 to model, due to the lack of data for the material composition near the  
 151 interface. Figure 2 illustrates the nanostructure of GO C-S-H and especially  
 152 the interface between the GO and the C-S-H [30]. The functional groups of  
 153 the GO sheet, mainly, oxygen atoms, react with the calcium atoms from the  
 154 C-S-H and form a strong interface. To determine the distance between the  
 155 calcium ion and the oxygen in carboxyl group, a DFT study was conducted  
 156 by Mehandzhiyski and co-workers [31]. The average length of Ca-O bond is  
 157 calculated as  $2.17 \text{ \AA}$ . In addition, the average distance between the calcium  
 158 layer and the carbon plane of the GO sheet can be obtained as  $2.17 + 1.66 =$   
 159  $3.83 \text{ \AA}$ . Moreover, the distance between the two calcium layers, surrounding  
 160 the GO sheet, can be derived as  $3.83 \times 2 = 7.66 \text{ \AA}$ .

161 ReaxFF has been used in hydrocarbons [33] and C-S-H structures [34, 35],  
 162 making it reasonable to model the GO cement. In general, ReaxFF can



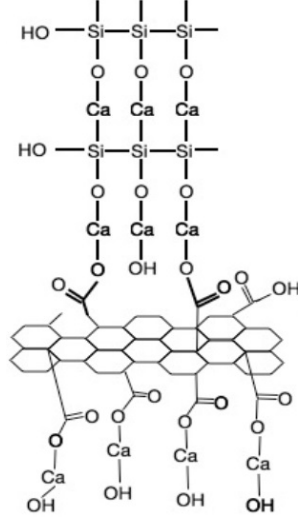


Figure 2: Illustration of GO cement composite at the nanoscale (reproduced from [32]).

163 simulate the chemical and physical interactions between Ca, Si, O, and H  
 164 atoms in the C-S-H gel, C, O, and H atoms in the GO, and Ca, Si, O, and  
 165 C atoms at the interface. The potential energy defined by the ReaxFF can  
 166 be expressed as [36]:

$$\begin{aligned}
 E_{\text{system}} = & E_{\text{bond}} + E_{\text{lp}} + E_{\text{over}} + E_{\text{under}} + E_{\text{val}} + E_{\text{pen}} \\
 & + E_{\text{coa}} + E_{\text{tors}} + E_{\text{conj}} + E_{\text{H-bond}} \\
 & + E_{\text{vdWaals}} + E_{\text{Coulomb}}
 \end{aligned} \tag{1}$$

167 where  $E_{\text{bond}}$  is bond energy,  $E_{\text{lp}}$  is long pair energy,  $E_{\text{over}}$  is over coordination  
 168 energy,  $E_{\text{under}}$  is under coordination energy,  $E_{\text{val}}$  is valence angle energy,  
 169  $E_{\text{pen}}$  is penalty energy,  $E_{\text{coa}}$  is three-body conjugation energy,  $E_{\text{tors}}$  is torsion  
 170 rotation energy,  $E_{\text{conj}}$  is four-body conjugation energy,  $E_{\text{H-bond}}$  is hydrogen  
 171 bond interaction energy,  $E_{\text{vdWaals}}$  is van der Waals interaction energy, and  
 172  $E_{\text{Coulomb}}$  is Coulomb interaction energy. The energy of per atom is calculated

173 by defined potentials from neighbor atoms. In the present study, not all of  
174 terms in Eq. (1) are considered necessary and some of them are set to zero.

175 The molecular structure of the GO reinforced C-S-H is shown in Figure 3.  
176 A vacuum space is set for technically allowing pulling out the GO sheet  
177 without extending the simulation box. In Figure 3, the blue atoms represent  
178 oxygen in water, the white atoms are hydrogen in water, and the green atoms  
179 represent calcium; the yellow atoms represent oxygen and the red atoms are  
180 silica, which form the silica chains, and the grey atoms are carbon and the  
181 pink atoms are oxygen forming the GO sheet. Periodic boundary conditions  
182 are applied in  $x$ - $z$  plane. The procedure to produce the molecular structure of  
183 GO C-S-H is as follows: a unit cell of C-S-H, which has the lattice parameters  
184 of  $a = 11.265 \text{ \AA}$ ,  $b = 7.386 \text{ \AA}$  and  $c = 10.931 \text{ \AA}$  with space group F2dd [21],  
185 is duplicated as  $3 \times 4 \times 1$  along  $x$ -,  $y$ -,  $z$ -directions, respectively.

186 The initial structure was relaxed for 50 ps in the isobaric-isothermal (NPT)  
187 ensemble. The Nosé-Hoover thermostat is used to keep the temperature at  
188 300 K, and the Nosé-Hoover barostat is used to maintain the pressure at  
189  $p = 0 \text{ Pa}$ . This was followed by a 50 ps run in the canonical (NVT) ensemble  
190 for a single layer of atoms where the Ca, Si, and oxygen in C-S-H are fixed.  
191 A time step of  $\Delta t = 0.25 \text{ fs}$  was used during the entire relaxation. LAMMPS  
192 [37] was used to perform the MD simulations.

193 After the initial relaxation, the system was subjected to the pull-out test.  
194 The outermost layer of atoms in C-S-H along  $y$ -direction was held fixed,  
195 while the outermost layer of carbon atoms (14 C atoms in total) in the  
196 GO sheet along  $y$ -direction was moved in the  $y$ -direction at a constant rate.  
197 Three pulling rates of the GO sheet were adopted:  $0.0016 \text{ \AA ps}^{-1}$ ,  $0.008 \text{ \AA ps}^{-1}$

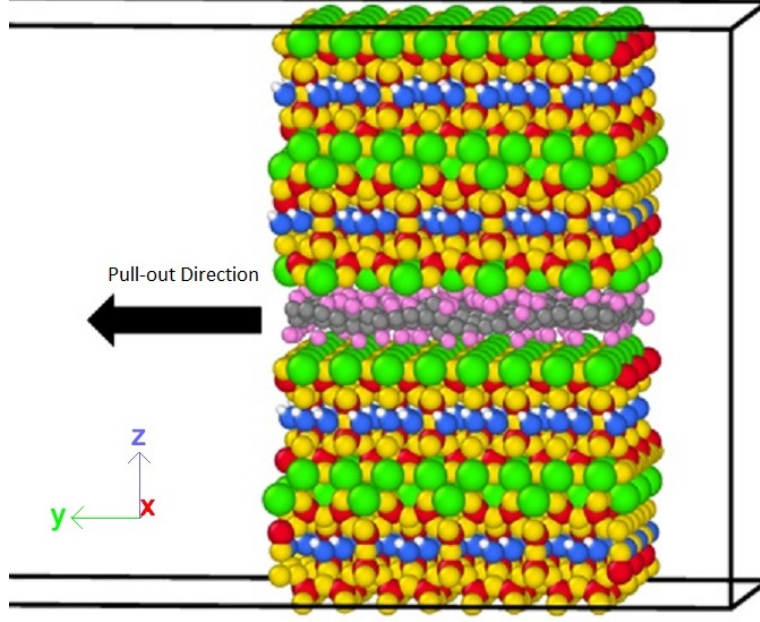


Figure 3: MD simulation cell for GO cement.

198 and  $0.08 \text{ \AA ps}^{-1}$ . After every  $0.4 \text{ \AA}$  pulling displacement of the GO sheet,  
 199 the system was relaxed for 2 ps. The relaxation period is chosen from the  
 200 literature [38]. A typical energy variation with time is shown in Figure 4, in  
 201 which an equilibrium or a convergence trends to be achieved. The data were  
 202 recorded during the relaxation before the next pull-out step was applied.  
 203 A cell incorporating a pure graphene sheet without functional groups was  
 204 also established for pull-out test, in light of comparing with the GO cement  
 205 and examining the effects of functional groups on the interfacial mechanical  
 206 properties. The interaction energy between GO sheet and C-S-H is calculated  
 207 and discussed, which represents the energy of the interface. The energy of  
 208 the carbon atoms from the GO sheet is also derived as a function of pulling

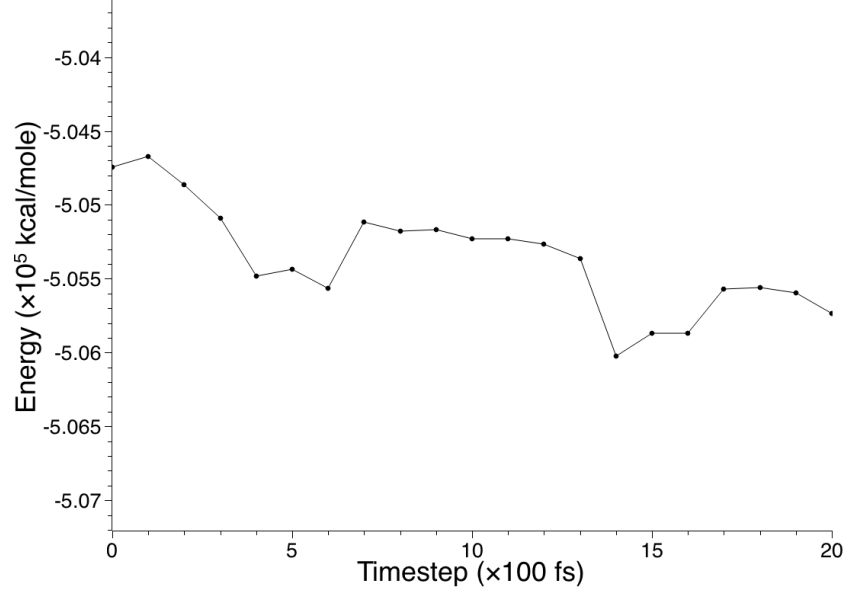


Figure 4: Energy - timestep curve during relaxation in pull-out process.

displacement under various pulling rates.

### 3. Results and discussion

The force  $\mathbf{F}_i$  exerted on atom  $i$  is given by

$$\mathbf{F}_i = -\frac{\partial E_i}{\partial \mathbf{r}_i} \quad (2)$$

where  $E_i$  is the interaction energy for atom  $i$ , and  $\mathbf{r}_i$  is the position of atom  $i$ . The relationship between the total force on the moving carbon atoms along pull-out direction ( $y$ -direction)  $F_y$  and the pull-out displacement for different loading rates are shown in [Figure 5](#). The pull-out force recorded is considered as being transferred to the interface between the GO sheet and the C-S-H matrix. Therefore, the force is directly related to the interfacial

218 stress transfer and can be used as the basis to derive the interfacial shear  
 219 strength of the nanocomposite.

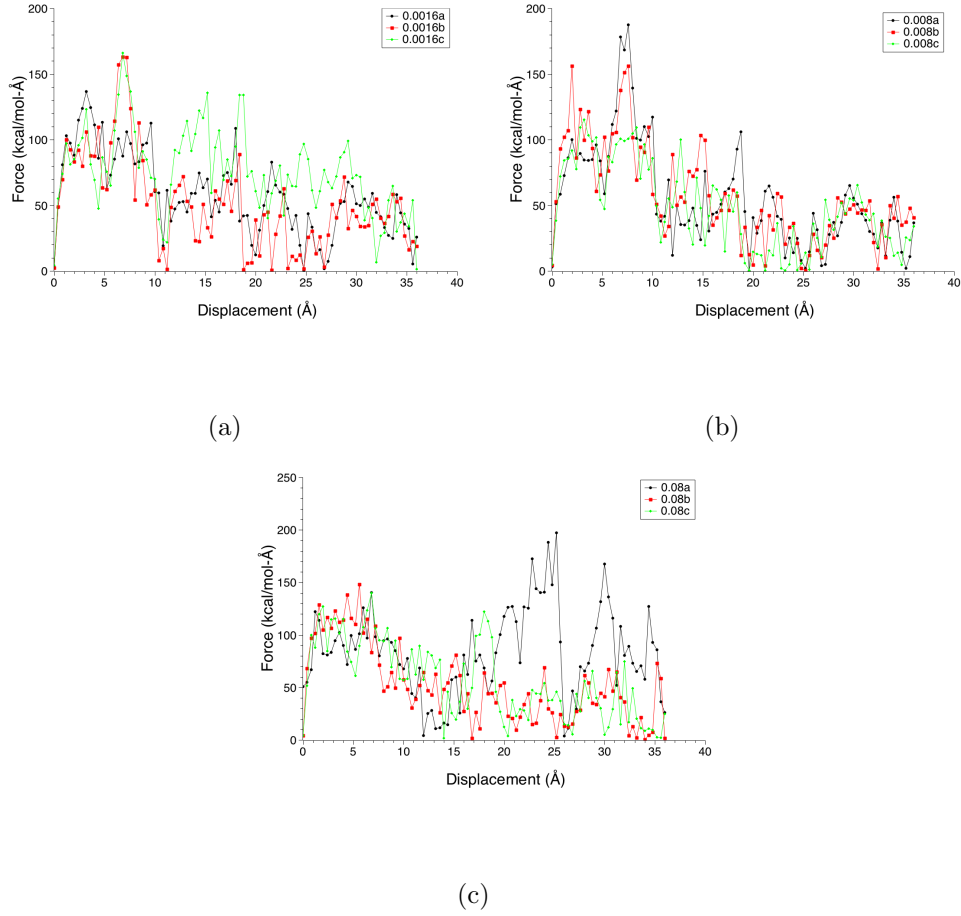


Figure 5: Pull-out force-displacement curves of GO cement under a pulling rate of: (a)  $0.0016 \text{ Å ps}^{-1}$ , (b)  $0.008 \text{ Å ps}^{-1}$  and (c)  $0.08 \text{ Å ps}^{-1}$

220 **Figure** 5 show the results for three groups of pull-out tests with different  
 221 pulling rates of the GO sheet ( $0.0016 \text{ Å ps}^{-1}$ ,  $0.008 \text{ Å ps}^{-1}$  and  $0.08 \text{ Å ps}^{-1}$ , re-  
 222 spectively). For each loading rate, three tests/simulations, as represented by  
 223 “a”, “b”, and “c” in the figures, were carried out to examine the repeatability

224 and reliability of the results. For all three loading rates, the results show no  
 225 significant difference for the initial elastic development (i.e., no bonds are broken).  
 226 The force then starts to fluctuate once bonds are stretched too much,  
 227 and bond breaking/reformation occurs. In addition, the force-displacement  
 228 relation under the loading rate of  $0.08 \text{ \AA ps}^{-1}$  has the largest fluctuation, especially  
 229 for the later pulling out stage, while the force-displacement relation  
 230 under the other loading rates has the smallest fluctuations. All three curves  
 231 for each loading rate are quite close to each other.

232 Figure 6 show the average force-displacement response; the error bars in  
 233 Figures 6(a)–6(c) from each loading rate are taken as the standard deviation  
 234 of the data in Figures 5(a)–5(c). Although the loading rate  $0.08 \text{ \AA ps}^{-1}$  has  
 235 slightly more fluctuations in the load-displacement curve, the overall/averaged  
 236 mechanical performance for all these three loading rates are similar. The averaged  
 237 pull-out forces are almost the same until about  $10 \text{ \AA}$ , after which there  
 238 are slightly more differences. Nevertheless, the first  $10 \text{ \AA}$  displacement represents  
 239 the initial cycle of the elastic-plastic-fracture phenomenon and thus  
 240 is more important than the following force development in the context of engineering  
 241 applications. It can be seen in Figures 6(a)–6(c) that three peaks  
 242 of the forces, representing three cycles of force development, are present during  
 243 the process of pulling out the GO sheet from the C-S-H matrix. In the  
 244 first  $2 \text{ \AA}$  displacement, the force increases rapidly, mainly due to the initial  
 245 elongation of C-O-Ca bonds. The force fluctuation follows before it reaches  
 246 its highest value (e.g.,  $140 \text{ kcal mol}^{-1} \text{ \AA}^{-1}$  for  $0.0016 \text{ \AA ps}^{-1}$  loading rate). In  
 247 this period, most of the bonds between the GO sheet and the C-S-H are  
 248 still intact, although some of have broken. After the peak load, the force

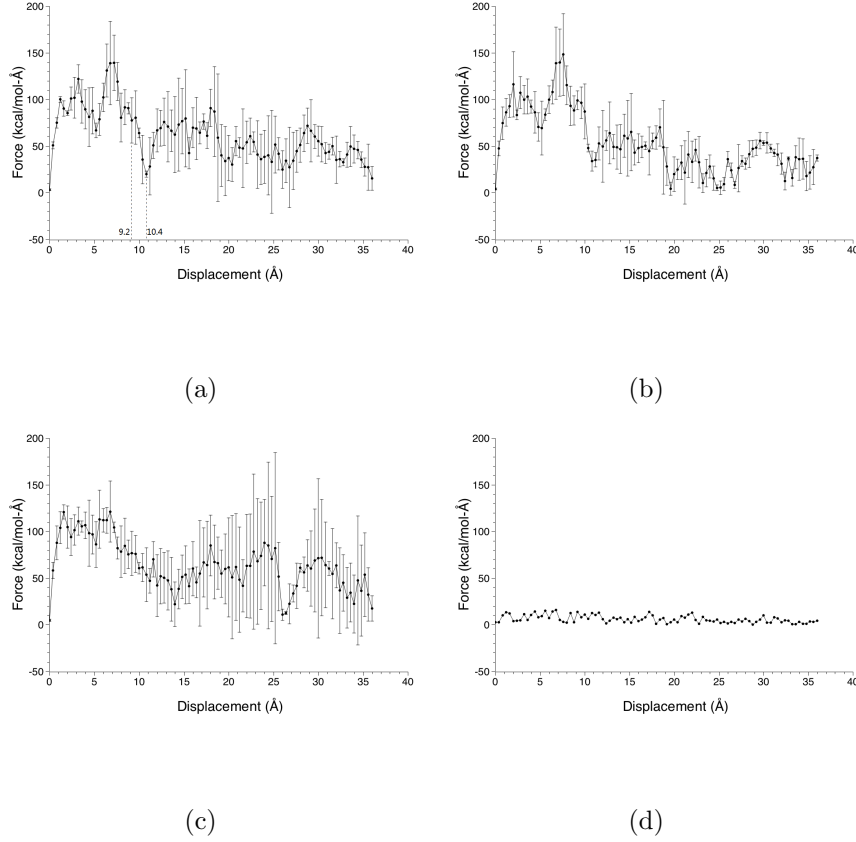


Figure 6: Averaged force-displacement curve of GO cement with a the pulling rate of: (a)  $0.0016 \text{ Å ps}^{-1}$  (b)  $0.008 \text{ Å ps}^{-1}$  (c)  $0.08 \text{ Å ps}^{-1}$  (d) graphene pulled out from cement with a pulling rate of  $0.08 \text{ Å ps}^{-1}$ .

249 abruptly drops to  $19.9 \text{ kcal mol}^{-1} \text{ Å}^{-1}$  for the loading rate of  $0.0016 \text{ Å ps}^{-1}$ .  
 250 During this stage, most bonds at the interface are broken. Meanwhile, new  
 251 bonds are generated during the relaxation in the displacement range of  $9.2 \text{ Å}$   
 252 to  $10.4 \text{ Å}$ . The whole period up to  $10.4 \text{ Å}$  displacement represents a complete  
 253 and initial cycle of the shearing load development at the interface (i.e., an  
 254 initial increase, a kind of interesting yielding phase prior to the peak load and  
 255 a decrease/softening phase until a small residual value). As mentioned, such

an elastic-plastic-fracture phenomenon has been first observed at nanoscale for GO cement composite and not yet been seen in the macroscale mechanical property.

After the first complete cycle of the shearing load development at the interface, the GO continues to be pulled out while new bonds are being created. For example, during the displacement from 10.4 Å to 18 Å under the 0.0016 Å ps<sup>-1</sup> loading rate, the force increases again up to 90.8 kcal mol<sup>-1</sup> Å<sup>-1</sup>, which is then followed by a rapid decrease to 30.3 kcal mol<sup>-1</sup> Å<sup>-1</sup> at 20.4 Å displacement. The maximum force is smaller than that of the first cycle. The reduction is mainly caused by the 12 Å length of GO sheet, which has been pulled out of the C-S-H matrix, resulting in fewer C-O-Ca bonds being generated. The rapid increase in energy around 18 Å also shows the generation of bonds, as illustrated in Figure 6(a). After the second drop to the lower level, the force distribution begins to fluctuate significantly; about half length of the GO sheet has been pulled out of the original position, thus the short-range interaction between the GO and the C-S-H contributes less and less in the following period, making the energy distribution in the interface more complex and changeable. The third cycle starts from 26 Å and terminates at 36 Å with a peak force of 71.6 kcal mol<sup>-1</sup> Å<sup>-1</sup> at 28.8 Å pull-out displacement. At this stage, the GO has been completely pulled out of the C-S-H matrix.

According to Amonton's law of adhesion [39], the friction force  $F$  is divided into two parts:  $F = \mu L + F_0$ , the external normal force  $L$  multiplied by the friction coefficient  $\mu$  and the internal force  $F_0$  impacted by the adhesion between the two surfaces. In this study,  $L$  continuously decreases due



281 to the reduction of the contact surface; the internal force  $F_0$  should initially  
 282 increase because of bond stretching and then decrease due to bond breakage.  
 283 The force-displacement generally follows Amonton's law for individual cycles.  
 284 The simulations clearly show both the chemical interaction (i.e. bonding) and  
 285 the physical interaction occurring at the interface between the GO and the  
 286 C-S-H).

287 To investigate the influence of the oxygen functional group on the in-  
 288 terfacial mechanical performance of GO cement, the pull-out test was con-  
 289 ducted for pure graphene cement composite. At the interface between the  
 290 pure graphene sheet and the C-S-H, there is no chemical or short-range in-  
 291 teraction and only long range interaction remains. Figure 6(d) shows the  
 292 force-displacement curve for pure graphene without functional groups under  
 293 a pulling rate of  $0.08 \text{ \AA ps}^{-1}$ . The force remains relatively constant, with a  
 294 maximum value of about  $16 \text{ kcal mol}^{-1} \text{ \AA}^{-1}$ . The peaks keep decreasing until  
 295 it is completely pulled from the C-S-H matrix. This demonstrates that the  
 296 chemical bonds formed between the C-S-H and GO have significantly increase  
 297 the shearing force transferring capacity, about 8.5 times for the maximum  
 298 force.

299 The interfacial interaction energy  $\Delta E$  is an important parameter that  
 300 reflects the energy state for the interface between GO and C-S-H, which can  
 301 be defined as follows:

$$\Delta E = E_{Total} - E_{GO} - E_{C-S-H} \quad (3)$$

302 where  $E_{Total}$  is the potential energy of the whole system,  $E_{GO}$  is the potential  
 303 energy of all the atoms in the GO sheet alone (i.e., C-C bonds and C-O bonds)  
 304 and  $E_{C-S-H}$  is the potential energy of C-S-H alone. The interaction energy

305 represents the interfacial energy including the binding effect of oxygen as  
 306 function groups.

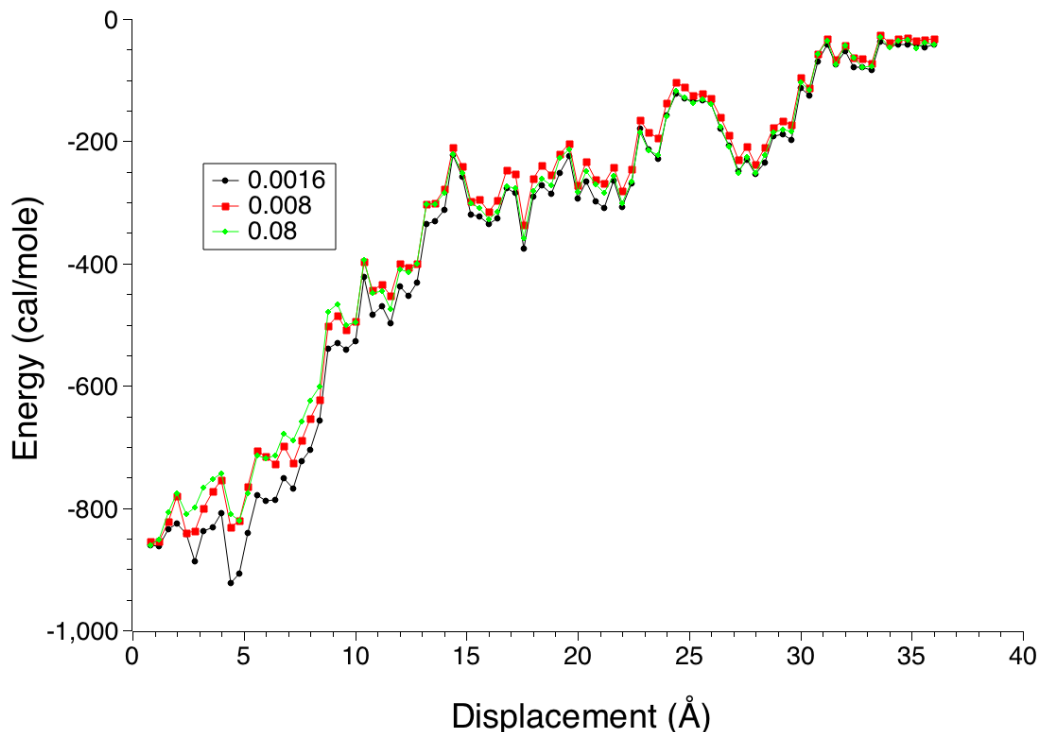


Figure 7: Interaction energy-displacement curves of GO cement with various pulling rates.

307 Figure 7 shows the interaction energy as a function of the pull-out dis-  
 308 placement for different loading rates. It should be noted that the energy is  
 309 shown with a sign, so the energy is actually decreasing rather than increasing  
 310 in magnitude. The interfacial energy decreases from  $850 \text{ cal mol}^{-1}$  to around  
 311  $50 \text{ kcal mol}^{-1}$  during the pull-out process. The energy loss of the interface is  
 312 mainly caused by the reduction of Ca-O-C chemical bonds. In Figure 7, all  
 313 three curves are initially constant for about  $4 \text{ Å}$  and then gradual decrease.  
 314 This demonstrates that there is no breakage of chemical bonds during the

315 first 4 Å of displacement. Further, the effect of the loading rates on the  
 316 change of interfacial energy is minimal.

317 The energies of all the carbon atoms in the GO sheet for different loading  
 318 scenarios are presented in Figures 8(a)–8(c). The energy of all carbon atoms  
 319 conforms to the trend of consistent increase in general for pulling rates of  
 320 0.0016 Å ps<sup>-1</sup> and 0.008 Å ps<sup>-1</sup>, despite some local decreases at certain load-  
 321 ing stages; there are three local decreases in the energy of all the carbon  
 322 atoms, and the three lowest local energies are exactly corresponding to the  
 323 three force peaks as illustrated in Figure 6(a), around 7 Å, 18 Å and 29 Å  
 324 respectively, for the 0.0016 Å ps<sup>-1</sup> pulling rate. Three tests were performed  
 325 for each loading rate, and the trend was clear and stable. This suggests  
 326 that these two pulling rates are suitable for pull-out test on GO cement  
 327 composites. However, the trend for the energy variation at the pulling rate  
 328 of 0.08 Å ps<sup>-1</sup> is unstable (see Figure 8(c)), and the error bars for most of  
 329 the curve are considerably larger. Compared to the energy variation of a  
 330 graphene sheet pulled out from C-S-H with a pulling rate 0.08 Å ps<sup>-1</sup> (see  
 331 Figure 8(d)), it can be confirmed that the oxygen atoms in GO sheet signifi-  
 332 cantly influence the pull-out process when the pulling rate is high. Therefore,  
 333 the choice of a proper loading rate for the pull-out test is key to reliable MD  
 334 simulation. A similar observation was made in Ref. 17, where different pulling  
 335 rates changed the material properties simulated from plastic to elastic.

336 With the pull-out force recorded, the pull-out shear stress can be calcu-  
 337 lated as [40]:

$$\tau = \frac{F}{A} \quad (4)$$

338 where  $F$  is the pull-out force, and  $A$  is the force-resisting area. The shear

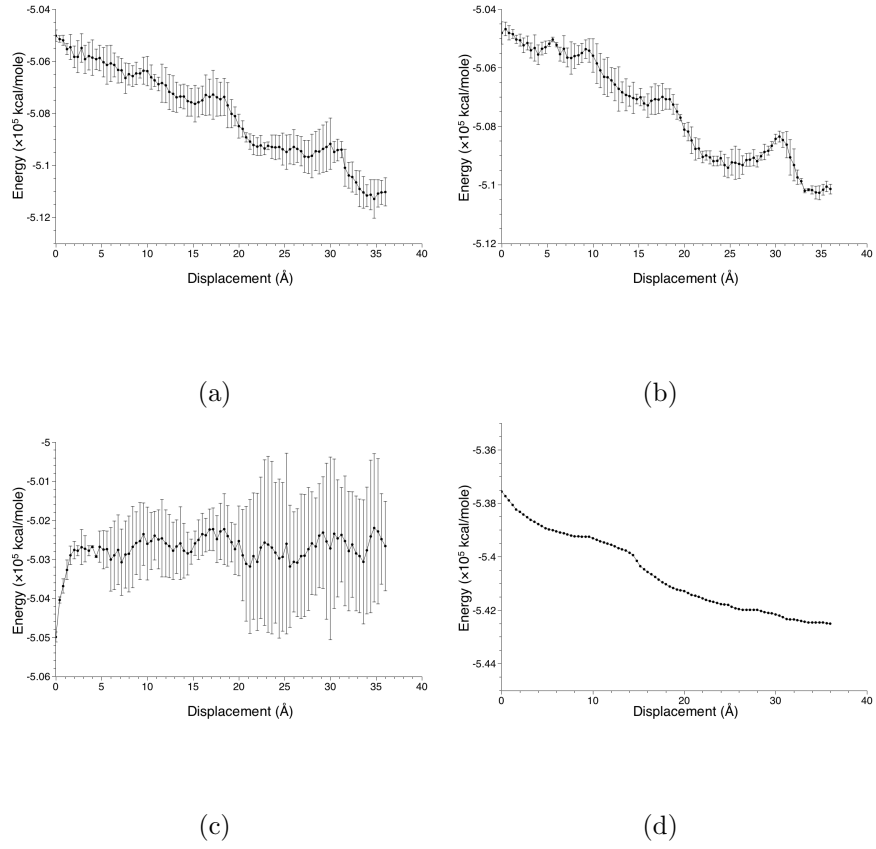


Figure 8: Averaged energy of carbon atoms as a function of pull-out displacement of GO cement with a pulling rate of: (a) 0.0016 Å ps<sup>-1</sup> (b) 0.008 Å ps<sup>-1</sup> (c) 0.08 Å ps<sup>-1</sup> (d) graphene pulled out from cement with a pulling rate of 0.08 Å ps<sup>-1</sup>.

339 stress  $\tau$  can be re-written as:

$$\tau = \frac{F}{A_{GO-CSH}} = \frac{F}{2|a_0 \times (b_0 - \Delta b)|} \quad (5)$$

340 where  $A_{GO-CSH}$  is the force-resisting area in the interface of C-S-H and GO  
 341 sheet,  $a_0$  is the length of GO sheet vertical to the pull-out direction,  $b_0$  is  
 342 the width of GO sheet along the pull-out direction, and  $\Delta b$  is the pull-out  
 343 distance of the GO sheet. In this model,  $a_0 = 32.13 \text{ \AA}$  and  $b_0 = 27.124 \text{ \AA}$ .

344 There are two sides of the GO sheet which are in shear, so the force-  
 345 resisting area is the double of the area of the GO sheet connecting to the  
 346 C-S-H. By using Eq. (5) and the values of  $a_0$  and  $b_0$  given above, the shear  
 347 stress can be calculated as a function of the pull-out displacement for the first  
 348 cycle. The pulling rate of  $0.0016 \text{ \AA ps}^{-1}$  is chosen. This relationship is shown  
 349 in Figure 9. It can be seen that the shear stress increases roughly until  
 350 400 MPa; the stress then fluctuates over the next about  $4 \text{ \AA}$  displacement  
 351 until the maximum shear stress is reached (i.e.,  $647.58 \pm 91.18 \text{ MPa}$  obtained  
 352 from different pulling rates). It is very interesting to find this fluctuation  
 353 is similar to stress yielding behavior which has not been commonly seen  
 354 in macroscale stress analysis. This stress yielding phase is then followed  
 355 by stress softening (i.e., stress decrease), which usually implies damage has  
 356 occurred. During the stress softening phase, the stress suddenly drops to  
 357 around 400 MPa and gradually decreases. This is similar to what have been  
 358 found in the macroscale Mode I and II fractures of cement, which has often  
 359 been simplified to a bilinear softening curve. At about  $10 \text{ \AA}$  displacement,  
 360 the shear stress drops to about 100 MPa which is comparable to that of the  
 361 pure graphene case.

362 The interfacial shear strength is calculated to be about  $647.58 \pm 91.18 \text{ MPa}$ .

363 As a general comparison, the tensile strength of the pure graphene sheet is  
 364 about 130 GPa [41], and the shear strength of Portland cement is typically in  
 365 the range of 6–35 MPa at the macroscale [42]. It would be extremely to verify  
 366 the results by comparing with experimental data; however, none is currently  
 367 available. As explained, this is probably because there is no experimental  
 368 method available for capturing the interfacial stress of the GO cement at  
 369 the nanoscale. However, this further increases the necessity of predicting the  
 370 interfacial mechanical properties by numerical approaches. It would be very  
 371 useful to have the nanoscale bond-slip relation including the shear strength  
 372 for GO cement which can be used as the inputs for multi-scale modeling or  
 373 to be upscaled to the engineering scale.

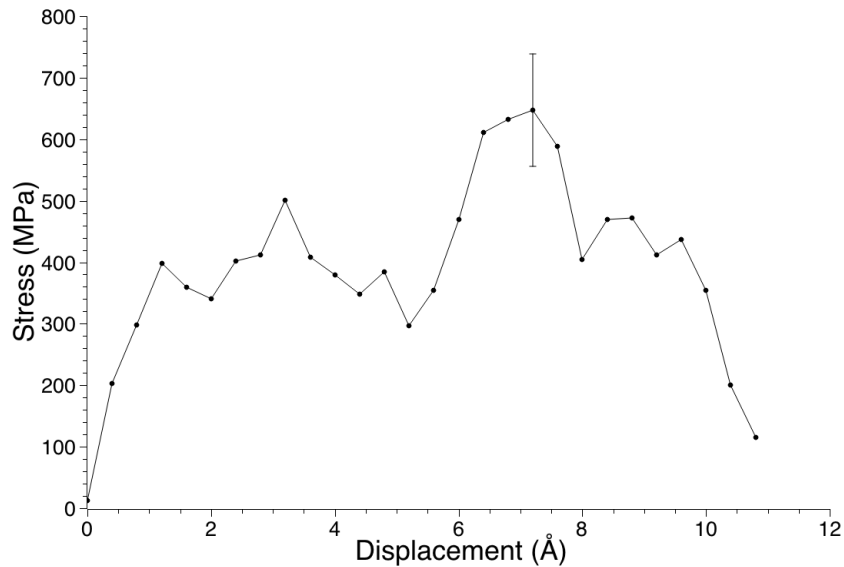


Figure 9: Average shear stress-displacement curve for GO cement.

374 The shear stress-displacement, often known as bond-slip relation, is for

the first time derived for GO cement. It has significant impact on multi-scale modeling (e.g., finite element simulation) in terms of the interface properties. The properties for interface elements in finite element analysis are usually not available due to the difficulties of experiments. This is why trial and error analysis is applied for determining the interfacial properties. The shear stress-displacement curve derived can well be used for defining the bond-slip behavior in the interface elements in multi-scale numerical simulation and also be upscaled to the engineering properties at macroscale.

#### 4. Conclusion

In this work, the nano interface between the C-S-H and GO has been modeled and the complete stress transferring mechanism has been studied using MD. The structures for the GO and the C-S-H have been clearly presented, and pull-out tests were carried out in a realistic manner. ReaxFF was employed to provide the interactive potentials for the whole molecular system. Three different pulling rates were employed in running the MD simulations and it has been found that  $0.08 \text{ \AA ps}^{-1}$  leads to larger fluctuation in the force-displacement curve, compared with  $0.0016 \text{ \AA ps}^{-1}$  and  $0.008 \text{ \AA ps}^{-1}$ , especially for the later pulling out stage. The full stress displacement curve which represents the mechanical properties of the GO cement interface has been derived and the shear strength has been found to be  $647.58 \pm 91.18 \text{ MPa}$ . The shear stress-displacement curve has, for the first time, been derived for GO cement which represents the bond-slip relation in finite element simulation. It can be concluded that MD simulation offers a unique insight into modeling the nanoscale mechanical properties of cementitious nanocompos-

400 ites which have not, yet, been determined by experiment.

## 400 Acknowledgments

401 Partial financial support from the European Commission Horizon 2020  
402 MARIE Skłodowska-CURIE Research and Innovation Staff Exchange scheme  
403 through the grant 645696 (i.e. REMINE project) is gratefully acknowledged.

## 404 References

- 405 [1] K. Sobhan, M. Mashnad, Tensile strength and toughness of soil-cement-  
406 fly-ash composite reinforced with recycled high-density polyethylene  
407 strips, *Journal of Materials in Civil Engineering* 14 (2) (2002) 177–184.
- 408 [2] M. A. Ali, A. J. Majumdar, D. L. Rayment, Carbon fibre reinforcement  
409 of cement, *Cement and Concrete Research* 2 (2) (1972) 201–212.
- 410 [3] W. Sonphuak, N. Rojanarowan, Strength improvement of fibre cement  
411 product, *International Journal of Industrial Engineering Computations*  
412 4 (4) (2013) 505–516.
- 413 [4] J. Claramunt, M. Ardanuy, J. A. García-Hortal, R. D. Tolêdo Filho,  
414 The hornification of vegetable fibers to improve the durability of cement  
415 mortar composites, *Cement and Concrete Composites* 33 (5) (2011) 586–  
416 595.
- 417 [5] S. Leonard, A. Bentur, Improvement of the durability of glass fiber  
418 reinforced cement using blended cement matrix, *Cement and concrete*  
419 *research* 14 (5) (1984) 717–728.



- 420 [6] J. Chen, S.-C. Kou, C.-S. Poon, Hydration and properties of nano-TiO  
421 2 blended cement composites, *Cement and Concrete Composites* 34 (5)  
422 (2012) 642–649.
- 423 [7] O. Onuaguluchi, D. K. Panesar, M. Sain, Properties of nanofibre re-  
424 inforced cement composites, *Construction and Building Materials* 63  
425 (2014) 119–124.
- 426 [8] R. Siddique, A. Mehta, Effect of carbon nanotubes on properties of  
427 cement mortars, *Construction and Building Materials* 50 (2014) 116–  
428 129.
- 429 [9] A. Geim, K. Novoselov, O. V. Yazyev, S. G. Louie, S. Ghosh, W. Bao,  
430 D. L. Nika, S. Subrina, E. P. Pokatilov, C. N. Lau, Nobel prize for  
431 graphene, *Nature Materials* 6 (2007) 183–192.
- 432 [10] H. Alkhateb, A. Al-Ostaz, A. H.-D. Cheng, X. Li, Materials genome  
433 for graphene-cement nanocomposites, *Journal of Nanomechanics and*  
434 *Micromechanics* 3 (3) (2013) 67–77.
- 435 [11] M. Saafi, L. Tang, J. Fung, M. Rahman, J. Liggat, Enhanced proper-  
436 ties of graphene/fly ash geopolymeric composite cement, *Cement and*  
437 *Concrete Research* 67 (2015) 292–299.
- 438 [12] S. Lv, S. Ting, J. Liu, Q. Zhou, Use of graphene oxide nanosheets to  
439 regulate the microstructure of hardened cement paste to increase its  
440 strength and toughness, *CrystEngComm* 16 (36) (2014) 8508–8516.
- 441 [13] H. J. Du, S. D. Pang, Transport of water and chloride ion in cement

- 442 composites modified with graphene nanoplatelet, in: Key Engineering  
443 Materials, Vol. 629, Trans Tech Publ, 2015, pp. 162–167.
- 444 [14] S. Lv, J. Liu, T. Sun, Y. Ma, Q. Zhou, Effect of go nanosheets on shapes  
445 of cement hydration crystals and their formation process, Construction  
446 and Building Materials 64 (2014) 231–239.
- 447 [15] R. Shahsavari, R. J.-M. Pellenq, F.-J. Ulm, Empirical force fields for  
448 complex hydrated calcio-silicate layered materials, Physical Chemistry  
449 Chemical Physics 13 (3) (2011) 1002–1011.
- 450 [16] W. Wu, A. Al-Ostaz, A. H.-D. Cheng, C. R. Song, Computation of  
451 elastic properties of portland cement using molecular dynamics, Journal  
452 of Nanomechanics and Micromechanics 1 (2) (2011) 84–90.
- 453 [17] D. Hou, T. Zhao, P. Wang, Z. Li, J. Zhang, Molecular dynamics study  
454 on the mode i fracture of calcium silicate hydrate under tensile loading,  
455 Engineering Fracture Mechanics 131 (2014) 557–569.
- 456 [18] Y. Li, Y. Liu, X. Peng, C. Yan, S. Liu, N. Hu, Pull-out simulations on  
457 interfacial properties of carbon nanotube-reinforced polymer nanocom-  
458 posites, Computational Materials Science 50 (6) (2011) 1854–1860.
- 459 [19] N. Ding, X. Chen, C.-M. L. Wu, X. Lu, Computational investigation  
460 on the effect of graphene oxide sheets as nanofillers in poly(vinyl alco-  
461 hol)/graphene oxide composites, The Journal of Physical Chemistry C  
462 116 (42) (2012) 22532–22538.
- 463 [20] F. Liu, N. Hu, H. Ning, Y. Liu, Y. Li, L. Wu, Molecular dynamics sim-  
464 ulation on interfacial mechanical properties of polymer nanocomposites

- 465 with wrinkled graphene, Computational Materials Science 108 (Part A)  
466 (2015) 160–167.
- 467 [21] S. Merlino, E. Bonaccorsi, T. Armbruster, The real structure of tober-  
468 morite 11 Å normal and anomalous forms, old character and polytypic  
469 modifications, European Journal of Mineralogy 13 (3) (2001) 577–590.
- 470 [22] I. Richardson, Tobermorite/jennite-and tobermorite/calcium hydroxide-  
471 based models for the structure of csh: applicability to hardened pastes  
472 of tricalcium silicate, -dicalcium silicate, portland cement, and blends  
473 of portland cement with blast-furnace slag, metakaolin, or silica fume,  
474 Cement and Concrete Research 34 (9) (2004) 1733–1777.
- 475 [23] R. J.-M. Pellenq, A. Kushima, R. Shahsavari, K. J. Van Vliet, M. J.  
476 Buehler, S. Yip, F.-J. Ulm, A realistic molecular model of cement hy-  
477 drates, Proceedings of the National Academy of Sciences 106 (38) (2009)  
478 16102–16107.
- 479 [24] I. G. Richardson, Model structures for c-(a)-sh (i), Acta Crystallograph-  
480 ica Section B: Structural Science, Crystal Engineering and Materials  
481 70 (6) (2014) 903–923.
- 482 [25] A. Lerf, H. He, M. Forster, J. Klinowski, Structure of graphite oxide  
483 revisited, The Journal of Physical Chemistry B 102 (23) (1998) 4477–  
484 4482.
- 485 [26] K. A. Mkhoyan, A. W. Contryman, J. Silcox, D. A. Stewart, G. Eda,  
486 C. Mattevi, S. Miller, M. Chhowalla, Atomic and electronic structure of  
487 graphene-oxide, Nano letters 9 (3) (2009) 1058–1063.

- 488 [27] J.-A. Yan, M. Chou, Oxidation functional groups on graphene: Struc-  
489 tural and electronic properties, *Physical review B* 82 (12) (2010) 125403.
- 490 [28] R. Lahaye, H. Jeong, C. Park, Y. Lee, Density functional theory study of  
491 graphite oxide for different oxidation levels, *Physical Review B* 79 (12)  
492 (2009) 125435.
- 493 [29] T. Dyer, N. Thamwattana, R. Jalili, Modelling the interaction of  
494 graphene oxide using an atomistic-continuum model, *RSC Advances*  
495 5 (94) (2015) 77062–77070.
- 496 [30] Z. Pan, L. He, L. Qiu, A. H. Korayem, G. Li, J. W. Zhu, F. Collins, D. Li,  
497 W. H. Duan, M. C. Wang, Mechanical properties and microstructure of  
498 a graphene oxidecement composite, *Cement and Concrete Composites*  
499 58 (2015) 140–147.
- 500 [31] A. Y. Mehandzhiyski, E. Riccardi, T. S. van Erp, H. Koch, P.-O.  
501 Åstrand, T. T. Trinh, B. A. Grimes, Dft study on the interactions of  
502 metal ions with long chain deprotonated carboxylic acids.
- 503 [32] A. Lerf, H. He, M. Forster, J. Klinowski, Structure of graphite oxide  
504 revisited, *The Journal of Physical Chemistry B* 102 (23) (1998) 4477–  
505 4482.
- 506 [33] K. Chenoweth, A. C. Van Duin, W. A. Goddard, Reaxff reactive force  
507 field for molecular dynamics simulations of hydrocarbon oxidation, *The*  
508 *Journal of Physical Chemistry A* 112 (5) (2008) 1040–1053.
- 509 [34] H. Manzano, S. Moeini, F. Marinelli, A. C. Van Duin, F.-J. Ulm, R. J.-  
510 M. Pellenq, Confined water dissociation in microporous defective sili-

- 511 cates: mechanism, dipole distribution, and impact on substrate prop-  
 512 erties, *Journal of the American Chemical Society* 134 (4) (2012) 2208–  
 513 2215.
- 514 [35] D. Hou, Z. Li, T. Zhao, Reactive force field simulation on polymerization  
 515 and hydrolytic reactions in calcium aluminate silicate hydrate (cash) gel:  
 516 structure, dynamics and mechanical properties, *RSC Advances* 5 (1)  
 517 (2015) 448–461.
- 518 [36] K. D. Nielson, A. C. van Duin, J. Oxgaard, W.-Q. Deng, W. A. God-  
 519 dard, Development of the reaxff reactive force field for describing tran-  
 520 sition metal catalyzed reactions, with application to the initial stages of  
 521 the catalytic formation of carbon nanotubes, *The Journal of Physical*  
 522 *Chemistry A* 109 (3) (2005) 493–499.
- 523 [37] S. Plimpton, Fast parallel algorithms for short-range molecular dynam-  
 524 ics, *Journal of computational physics* 117 (1) (1995) 1–19.
- 525 [38] S.-H. Cheng, C. Sun, Size-dependent fracture toughness of nanoscale  
 526 structures: crack-tip stress approach in molecular dynamics, *Journal of*  
 527 *Nanomechanics and Micromechanics* 4 (4) (2013) A4014001.
- 528 [39] J. Gao, W. Luedtke, D. Gourdon, M. Ruths, J. Israelachvili, U. Land-  
 529 man, Frictional forces and amontons’ law: from the molecular to the  
 530 macroscopic scale, *The Journal of Physical Chemistry B* 108 (11) (2004)  
 531 3410–3425.
- 532 [40] A. P. Borei, R. J. Schmidt, O. M. Sidebottom, *Advanced mechanics of*  
 533 *materials*, Vol. 6, Wiley New York, 1993.

- 534 [41] C. Lee, X. Wei, J. W. Kysar, J. Hone, Measurement of the elastic prop-  
535 erties and intrinsic strength of monolayer graphene, *Science* 321 (5887)  
536 (2008) 385–388.
- 537 [42] M. Moosavi, W. F. Bawden, Shear strength of portland cement grout,  
538 *Cement and Concrete Composites* 25 (7) (2003) 729–735.